

A relation between the characteristic stellar ages of galaxies and their intrinsic shapes

Jesse van de Sande^{1*}, Nicholas Scott^{1,2}, Joss Bland-Hawthorn¹, Sarah Brough^{2,3}, Julia J. Bryant^{1,2,4}, Matthew Colless^{2,5}, Luca Cortese⁶, Scott M. Croom^{1,2}, Francesco d'Eugenio^{2,5}, Caroline Foster^{1,7}, Michael Goodwin⁴, Iraklis S. Konstantopoulos^{4,8}, Jon S. Lawrence⁴, Richard M. McDermid^{4,9}, Anne M. Medling^{5,10}, Matt S. Owers^{4,9}, Samuel N. Richards¹¹ and Rob Sharp^{2,5}

Stellar population and stellar kinematic studies provide unique but complementary insights into how galaxies build-up their stellar mass and angular momentum¹⁻³. A galaxy's mean stellar age reveals when stars were formed, but provides little constraint on how the galaxy's mass was assembled. Resolved stellar dynamics⁴ trace the change in angular momentum due to mergers, but major mergers tend to obscure the effect of earlier interactions⁵. With the rise of large multi-object integral field spectroscopic surveys, such as SAMI⁶ and MaNGA⁷, and single-object integral field spectroscopic surveys (for example, ATLAS^{3D} (ref. ⁸), CALIFA⁹, MASSIVE¹⁰), it is now feasible to connect a galaxy's star formation and merger history on the same resolved physical scales, over a large range in galaxy mass, morphology and environment^{4,11,12}. Using the SAMI Galaxy Survey, here we present a combined study of spatially resolved stellar kinematics and global stellar populations. We find a strong correlation of stellar population age with location in the $(V/\sigma, \epsilon_e)$ diagram that links the ratio of ordered rotation to random motions in a galaxy to its observed ellipticity. For the large majority of galaxies that are oblate rotating spheroids, we find that characteristic stellar age follows the intrinsic ellipticity of galaxies remarkably well.

Using data from the Sydney–Australian Astronomical Observatory (AAO) Multi-object Integral field spectrograph (SAMI) Galaxy Survey, we measure the spatially resolved stellar rotation V (km s^{-1}), stellar velocity dispersion σ (km s^{-1})¹¹ and global stellar population luminosity-weighted age (Gyr)¹². Stellar masses are derived from the relation between optical $g-i$ colour, i -band luminosity and stellar mass. Our sample of 843 galaxies covers a broad range in stellar mass ($9.5 < \log(M/M_\odot) < 11.6$), and the full range in optical morphology (E–Sd) and large-scale environment (field cluster).

In Fig. 1, we present our stellar kinematic measurements $(V/\sigma)_e$ as a function of stellar mass. $(V/\sigma)_e$ quantifies the ratio between ordered rotation and random orbital motion in a galaxy and is defined as the square root of the ratio of the luminosity-weighted V^2 and σ^2 within an ellipse that encloses half of the projected total galaxy light (equation (1))^{13,14}. We colour code the data by the

luminosity-weighted stellar age measured from an integrated spectrum within the same effective elliptical aperture for which the stellar kinematics are derived. There is a strong relation between $(V/\sigma)_e$ and age, such that galaxies with young stellar populations (age < 2.5 Gyr, blue) are predominantly rotationally supported (mean $(V/\sigma)_e = 0.58$), whereas galaxies with old stellar populations (age > 10 Gyr, red) are more pressure supported by random orbital motion of stars (mean $(V/\sigma)_e = 0.23$).

While the relation between age and $(V/\sigma)_e$ is stronger than the relation between age and stellar mass (Supplementary Fig. 1), both relations still leave a large residual. In Fig. 2, we investigate the connection between age and stellar dynamical properties further. We show the $(V/\sigma, \epsilon_e)$ diagram for galaxies, which relates the ratio of ordered to random motion $(V/\sigma)_e$ to the observed ellipticity ϵ_e . As well as colour coding galaxies by their individual ages in Fig. 2a, we now also use a locally weighted regression algorithm (LOESS¹⁵) to recover the mean underlying trend in the sample, as shown in Fig. 2b. In addition, we show theoretical predictions from the tensor virial theorem that links velocity anisotropy, rotation and intrinsic shape¹³. We use the best-fitting relation from a high-quality subset of galaxies from the SAURON sample $\beta_z = 0.6 \pm 0.1 \times \epsilon_{\text{intr}}$ (ref. ¹⁴) (where β_z is the anisotropy and ϵ_{intr} is the intrinsic ellipticity), that is, we assume that all galaxies are mildly anisotropic. An axisymmetric, oblate rotating spheroid with varying intrinsic ellipticity and anisotropy, when observed edge-on, is shown as a solid magenta line¹⁴. On this line, nearly round spherical galaxies reside on the bottom left; flattened rotating disks are on the top right. The dashed lines show galaxies with constant intrinsic ellipticities, but observed with varying viewing angle from face-on (zero ellipticity) to edge-on (towards the magenta line).

LOESS smoothing reveals that the age of a stellar population follows the lines of different projected intrinsic ellipticities remarkably well; along a line of constant intrinsic ellipticity, smoothed age is nearly constant. As the shape and kinematic properties of the galaxies transform from dynamically cold and intrinsically flat into dynamically hotter, pressure-supported, thicker, oblate spheroids, the mean age of the stellar population is seen to increase. On the bottom left part of the diagram, we find maximally old, fully dispersion-dominated, nearly spherical galaxies.

¹Sydney Institute for Astronomy, School of Physics, The University of Sydney, Sydney, New South Wales, Australia. ²ARC Centre of Excellence for All-sky Astrophysics (CAASTRO), The University of Sydney, Sydney, New South Wales, Australia. ³School of Physics, University of New South Wales, Sydney, New South Wales, Australia. ⁴Australian Astronomical Observatory, North Ryde, New South Wales, Australia. ⁵Research School of Astronomy and Astrophysics, Australian National University, Canberra, Australian Capital Territory, Australia. ⁶International Centre for Radio Astronomy Research, The University of Western Australia, Crawley, Western Australia, Australia. ⁷ARC Centre of Excellence for All-sky Astrophysics in 3 Dimensions (ASTRO 3D), The University of Sydney, Sydney, New South Wales, Australia. ⁸Atlassian, Sydney, New South Wales, Australia. ⁹Department of Physics and Astronomy, Macquarie University, Sydney, New South Wales, Australia. ¹⁰Cahill Center for Astronomy and Astrophysics California Institute of Technology, Pasadena, CA, USA. ¹¹SOFIA Operations Center, USRA, NASA Armstrong Flight Research Center, Palmdale, CA, USA. *e-mail: jesse.vandesande@sydney.edu.au

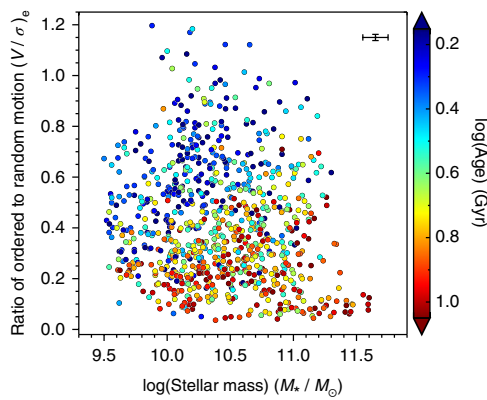


Fig. 1 | Ratio between stellar ordered rotation and random orbital motion in a galaxy $(V/\sigma)_e$ as a function of total stellar mass. Data are colour coded by the luminosity-weighted stellar population age within one effective radius. The median uncertainty on $(V/\sigma)_e$ and M_* is shown in the top-right corner; the median uncertainty on $\log(\text{age})$ is ± 0.15 dex.

We simulate the minimum required sample size for detecting this trend, by randomly drawing galaxies from our full sample of 843 galaxies, and then repeating the LOESS smoothing on that subsample. The relation between age and intrinsic ellipticity becomes visible with a minimum number of ~ 250 galaxies, but only if the sample has a full range in visual morphology.

There is no dependency on stellar mass within the $(V/\sigma, \epsilon_e)$ diagram for all galaxies that are consistent with being axisymmetric, rotating, oblate spheroids (above magenta line), though galaxies with the highest stellar mass are more likely to be pressure-supported spheroids than rotating (Supplementary Figs. 2 and 3).

It is important to emphasize that this newly discovered relation extends beyond the general notion that ‘disks are young’ and ‘bulges are old’. First, $(V/\sigma)_e$ is the more accurate, physically motivated and dynamical equivalent of the morphological bulge-to-disk ratio measurements that are notoriously difficult¹⁶ and hampered by inclination and dust extinction. Second, bulge-to-disk decompositions have revealed a wide distribution of the Sérsic index for both bulges and disks, but more importantly, have demonstrated that bulges can have blue colours while disks can be red, and that decomposed early-type bulges and disks have the same colour distribution¹⁶. Third, optical morphology is not an ideal tracer of the underlying dynamical structure for early-type galaxies¹⁷, as a large fraction of galaxies with elliptical morphology have high $(V/\sigma)_e$ values⁴. Fourth, we recover the same relation for low mass galaxies ($\log(M_*/M_\odot) < 10.25$, Supplementary Fig. 2), where we find a negligible number of galaxies with a classical, dispersion-dominated bulge.

To remove any doubt that the observed relation between age and intrinsic ellipticity is due to our large range in optical morphology, we now separate our sample into early-type (Fig. 3a) and late-type (Fig. 3b) galaxies. Our results confirm the well-known fact that early-type galaxies are on average older, more spherical and more dispersion-dominated than late-type galaxies. Within the early- and late-type morphological samples, the LOESS smoothed trends are consistent with the trend of the full sample: young stellar populations reside in rapidly rotating, intrinsically flat galaxies, and older stellar populations are found in more spherical and pressure-supported galaxies. The trend between age and intrinsic shape also remains if we only select S0 and early spiral galaxies.

To quantify this relation further, in Fig. 4, we deproject our observed $(V/\sigma, \epsilon_e)$ data onto the intrinsic ellipticity–inclination plane, using the theoretical model predictions for rotating, oblate, axisymmetric spheroids with varying intrinsic shape and anisotropy.

Galaxies below the magenta line are excluded from the sample because they are outside the model range, which excludes the majority of slow-rotating galaxies¹⁷, which are typically massive with old stellar populations (see Fig. 1). Furthermore, we exclude near-perfectly round galaxies ($\epsilon_e < 0.025$) for which the model predictions are highly degenerate and the relative measurement uncertainties on ϵ_e are large. Our deprojection approach is supported by an independent method for determining the intrinsic ellipticity from inverting the distributions of apparent ellipticities and kinematic misalignments that show that the intrinsic ellipticity agrees well with the theoretical model prediction¹⁸.

After deprojecting the data, we still find that stellar age follows the intrinsic ellipticity remarkably well, with no effect on inclination. For low inclination, the LOESS smoothing suggests a slight deviation in the age–intrinsic ellipticity relation. However, for these galaxies, which are observed nearly face-on, the deprojection is more uncertain because the model tracks in the $(V/\sigma, \epsilon_e)$ plane are closest together. We note that the relation between anisotropy and intrinsic ellipticity is a key ingredient in the deprojection. However, the relation between age and intrinsic ellipticity does not change within the anisotropic uncertainty, and only in the extreme case of no anisotropy ($\beta_z = 0$) do we start to see a mild deviation of the horizontal age trend in Fig. 4. Axisymmetric Jeans anisotropic modelling or more flexible Schwarzschild modelling are required to simultaneously constrain the intrinsic ellipticity and anisotropy, but this is beyond the scope of this study.

We show the relation between age and intrinsic ellipticity in Fig. 4c. The contour reveals a curved relation, yet the root-mean-square (RMS) scatter in $\log(\text{age})$ from a best-fitting linear and quadratic function are the same (0.238 dex). Early- and late-type galaxies reside at opposite sides of the relation, but in the region of overlap show consistent age and intrinsic ellipticity values. When using different aperture sizes (0.5, 1.0 and 2.0 R_e , where R_e is the semi-major effective radius of the galaxy), we find consistent results, which indicates that the relation between age and intrinsic ellipticity is not influenced by aperture effects.

Due to our broad range in stellar mass, optical morphology and large-scale environment, our results provide strong constraints on how galaxies build-up their stellar mass and angular momentum. The formation and growth of a bulge due to mergers will lower $(V/\sigma)_e$ and ϵ_e , but increase the mean intrinsic ellipticity as a function of time^{4,19}. Secular evolutionary processes, such as bar formation through dynamical instabilities, also change the observed $(V/\sigma)_e$ and ellipticity distribution of galaxies over time¹⁹; the stellar velocity dispersion is observed to increase with bar strength²⁰. Thus, both mergers and secular evolution can explain, at least partially, the relation between age and intrinsic ellipticity observed in the SAMI Galaxy Survey data.

For early-type galaxies, the relation between age and intrinsic ellipticity is consistent with predictions from hydrodynamical cosmological simulations and observations at redshift $z \sim 2-3$ when the Universe was only three billion years old. Massive ($\log(M_*/M_\odot) > 11$) quiescent galaxies at high-redshift have significantly higher effective stellar velocity dispersions and effective densities compared with similar present-day galaxies²¹. Due to the surprising compactness of these galaxies in the early Universe²², obtaining stellar rotation measurements has only been possible for extremely rare, strongly gravitationally lensed galaxies²³. The handful of stellar rotation curve measurements at these redshifts suggest that massive red- and dead galaxies at $z \sim 2-3$ are still rapidly rotating. Both major and minor mergers are predicted to make these galaxies intrinsically more spherical and dynamically more pressure supported⁷. While dry minor mergers are required to explain the strong evolution in size, dry major mergers are most effective at creating slow-rotating dispersion-dominated galaxies²⁴. This picture is consistent with

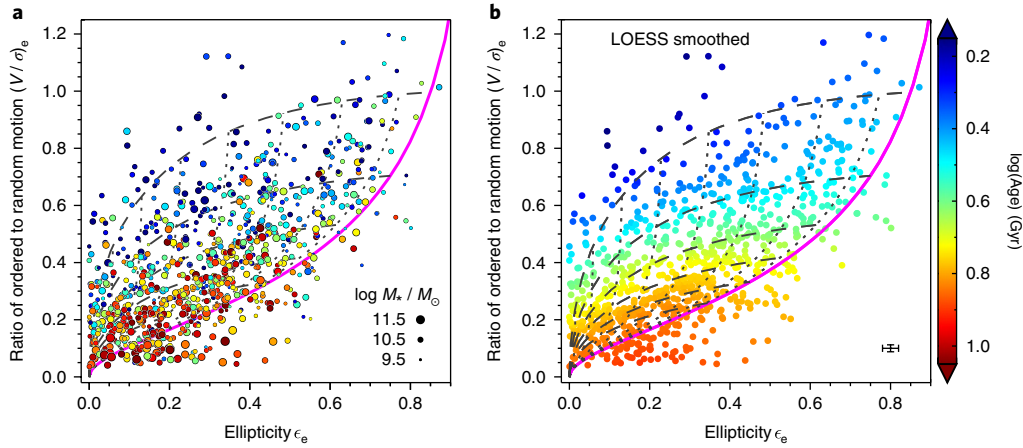


Fig. 2 | Linking stellar dynamics $(V/\sigma)_e$ and observed shape (ellipticity ϵ_e) with luminosity-weighted stellar age within one effective radius. **a, The colour coding reflects young (blue) and old (red) stellar population age of each individual galaxy and symbol size indicates the total stellar mass of the galaxy. **b**, Using the LOESS smoothing algorithm to recover the mean underlying trend in age. The median uncertainty on $(V/\sigma)_e$ and ϵ_e is shown in the bottom-right corner of **b**, and the median uncertainty on $\log(\text{age})$ is ± 0.15 dex. Theoretical predictions for the edge-on view of axisymmetric galaxies with anisotropy $\beta_z = 0.6 \times \epsilon_{\text{intr}}$ are shown as the solid magenta line¹⁴. The dotted lines show the model with different viewing angles from edge-on (magenta line) to face-on (towards zero ellipticity). Galaxies with different intrinsic ellipticities $\epsilon_{\text{intr}} = 0.85\text{--}0.35$ (top to bottom) are indicated by the dashed lines.**

the relation between age, $(V/\sigma)_e$ and ϵ_{intr} that we find in the SAMI Galaxy Survey early-type population: older stellar populations are more likely to reside in massive, more dispersion-dominated and more spherical systems, that can only form through dramatic interactions that are more common in the early Universe.

In the Milky Way, recent studies suggest that the Galactic thick disk is distinct from the dominant thin disk in abundance ratios and age²⁵. The younger, thin-disk stars are on near-circular, co-rotational orbits with a low velocity dispersion²⁶, whereas the thick disk with higher dispersion²⁷ is suggested to arise from a combination of stellar migration and/or flaring of the old disk stars²⁸. Some doubt remains as to whether the thick and thin disks are separate entities or a continuous distribution, but the parallels to the work presented here are striking. Within the SAMI sample, we find a similar trend where older stellar populations are in intrinsically thicker structures.

These present-day, dynamically hot galaxies could also be descendants of high-redshift disks that exhibit large random motions²⁹

and are geometrically thick³⁰. For rotation-dominated disks, the observed velocity dispersion of the ionized H α gas decreases by a factor of two over a period of 3.5 Gyr from $z \sim 2.3$ to $z \sim 0.9$ (ref. ³¹). As H α is a direct tracer of star formation, this suggests that as the Universe ages, newly formed stellar populations are more likely to reside in colder rotating disks, conforming with our findings here.

In this study, we have shown a relation between the intrinsic shape and stellar population age of galaxies, by combining imaging, spatially resolved dynamics and stellar population measurements. This shows the power of utilizing integral field spectroscopy on a large sample of galaxies to further our understanding of physical processes involved in the build-up of stellar mass and angular momentum in galaxies.

Methods

The SAMI Galaxy Survey. The SAMI⁶ is mounted at the prime focus on the Anglo-Australian Telescope. SAMI uses 13 fused-fibre bundles (hexabundles^{32,33}) with a

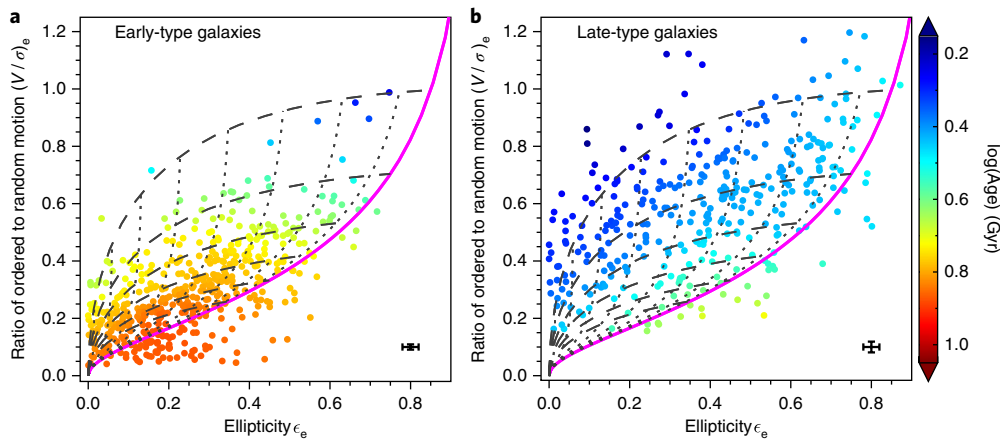


Fig. 3 | Luminosity-weighted stellar age in the $(V/\sigma)_e$, ϵ_e diagram, split by visual morphological type. **a, **b**, Galaxies with early-type morphology (elliptical and S0; **a**) and galaxies with late-type morphology (Sa–Sd and irregular; **b**). The colour coding highlights the LOESS smoothed stellar population ages. The LOESS algorithm is applied separately to the two individual subsamples. Lines shown are the same as in Fig. 2. The median uncertainty on $(V/\sigma)_e$ and ϵ_e is shown in the bottom-right corner of **b**, and the median uncertainty on $\log(\text{age})$ is ± 0.15 dex.**

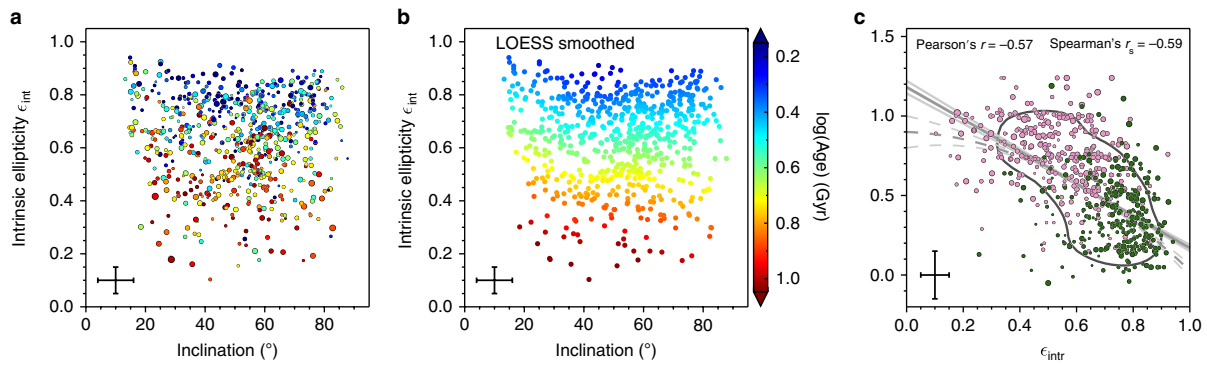


Fig. 4 | Intrinsic ellipticity and inclination derived from theoretical predictions and our data from within the $(V/\sigma, \epsilon_e)$ diagram. Only galaxies that are consistent with being axisymmetric rotating spheroids, and with $\epsilon_e > 0.025$ are included in the sample. In each panel, we show the median uncertainty in the bottom-left corner. **a**, The colour coding reflects the stellar population age of individual galaxies and symbol size indicates the total stellar mass of the galaxy. **b**, Using the LOESS smoothing algorithm to recover the mean underlying trend in age. **c**, Relation between age and intrinsic ellipticity for early-type (pink) and late-type (green) galaxies. The contour encloses 68% of the total probability using kernel density estimates. The solid line shows the best-fitting relation of $\log(\text{age}) = -1.01 \pm 0.06 \times \epsilon_{\text{intr}} + 1.18 \pm 0.04$, with an RMS scatter in $\log(\text{age})$ of 0.238 dex, using the Interactive Data Language (version 8.4; www.harrisgeospatial.com/SoftwareTechnology/IDL.aspx) LINMIX_ERR function that uses a Bayesian approach to linear regression. The dashed line shows the best-fitting relation $\log(\text{age}) = 0.80 \pm 0.28 \times \epsilon_{\text{intr}}^2 - 0.07 \pm 0.34 \times \epsilon_{\text{intr}} + 0.90 \pm 0.10$ using the POLY_FIT function, with an RMS scatter in $\log(\text{age})$ of 0.238 dex. The Pearson's and Spearman's rank correlation coefficients are given at the top of **c**.

high (75%) fill factor, deployable over a 1° diameter field of view. Each hexabundle contains 61 fibres of $1.6''$ angle on sky, resulting in each integral field unit covering an $\sim 15''$ diameter region on the sky. The integral field units, as well as 26 individual sky fibres, are plugged into pre-drilled plates using magnetic connectors. SAMI fibres are fed to the double-beam AAOmega spectrograph³⁴. AAOmega allows a range of different resolutions and wavelength ranges. For the SAMI Galaxy Survey, the 580 V and 1,000 R grating are used in the blue (3,750–5,750 Å) and red (6,300–7,400 Å) arm of the spectrograph, respectively. This results in a resolution of $R_{\text{blue}} \sim 1,810$ ($\sigma \sim 70 \text{ km s}^{-1}$) at 4,800 Å, and $R_{\text{red}} \sim 4,260$ ($\sigma \sim 30 \text{ km s}^{-1}$) at 6,850 Å (ref. ¹¹).

The SAMI Galaxy Survey^{6,35} aims to observe 3,600 galaxies, covering a broad range in galaxy stellar mass ($M_* = 10^8$ – $10^{12} M_\odot$) and galaxy environment (field, groups and clusters). Field and group targets were selected from four volume-limited galaxy samples derived from cuts in stellar mass in the Galaxy and Mass Assembly (GAMA³⁶) G09, G12 and G15 regions. Cluster targets were obtained from eight high-density cluster regions sampled within radius R_{200} with the same stellar mass limit as for the GAMA fields³⁷. Observations of the data presented here were carried out between January 2013 and June 2015. Reduced data are presented as three-dimensional data cubes (two spatial, one spectral dimension) with a spatial sampling of $0.5''$ (ref. ³⁸). The data have a median seeing of $2.1''$ (ref. ³⁹).

Ancillary data. We use the multi-Gaussian expansion^{40–42} technique to derive effective radii, ellipticities and position angles, using imaging data from GAMA-SDSS (Galaxy And Mass Assembly, Sloan Digital Sky Survey)³⁶, SDSS¹³ and VST (VLT (Very Large Telescope) Survey Telescope)^{37,44}. R_e is defined as the semi-major axis effective radius, and the ellipticity of the galaxy within one effective radius as ϵ_e , measured from the best-fitting multi-Gaussian expansion model. Visual morphological classifications were performed on the SDSS and VST colour images; late- and early-types are divided according to their shape, presence of spiral arms and/or signs of star formation⁴⁵. Stellar mass estimates M_* are obtained from the rest-frame i -band absolute magnitude and g - i colour by using a colour–mass relation^{35,46}. A Chabrier stellar initial mass function⁴⁷ and exponentially declining star formation histories are assumed.

Stellar kinematics. We measure the stellar kinematic parameters from the SAMI data¹¹ by fitting the spectra with the penalized pixel-fitting code (pPXF⁴⁸), assuming a Gaussian line of sight velocity distribution (LOSVD), that is, extracting only the stellar velocity V and stellar velocity dispersion σ . The SAMI blue and red spectra (convolved to a common spectral resolution) are rebinned onto a logarithmic wavelength scale with constant velocity spacing (57.9 km s^{-1}), using the code LOG_REBIN provided with the pPXF package. Annular binned spectra are used to derive local optimal templates. For building templates, we use the MILES stellar library⁴⁹, which consists of 985 stars with large variety in stellar atmospheric parameters.

After constructing annular optimal templates, we run pPXF three times on each galaxy spaxel. The first fit is used for determining a precise measure of the noise scaling from the residual of the fit. A 12th-order additive Legendre polynomial is used to remove residuals from small errors in the flux calibration. In the second fit, we mask the emission lines and clip outliers using the CLEAN parameter in pPXF. The velocity and velocity dispersion

are extracted from the third and final fit. In the last step, pPXF is fed with the optimal templates from the annular bin in which the spaxel is located, plus the optimal templates from adjacent annular bins. Uncertainties on the LOSVD parameters are estimated from 150 simulated spectra. For each spaxel, we estimate the uncertainties on the LOSVD parameters from the residuals of the best-fit minus the observed spectrum. These residuals are then randomly rearranged in wavelength and added to the best-fit template. We refit this simulated spectrum with pPXF, and the process is then repeated 150 times. The uncertainties on the LOSVD parameters are the standard deviations of the resulting simulated distributions.

From the unbinned flux, velocity and velocity dispersion maps, we derive $(V/\sigma)_e$ within an elliptical aperture with semi-major axis R_e and axis ratio b/a , using the following definition¹⁴:

$$\left(\frac{V}{\sigma}\right)_e^2 \equiv \frac{\langle V^2 \rangle}{\langle \sigma^2 \rangle} = \frac{\sum_{i=0}^{N_{\text{spx}}} F_i V_i^2}{\sum_{i=0}^{N_{\text{spx}}} F_i \sigma_i^2} \quad (1)$$

The subscript i refers to the spaxel position within the ellipse, F_i the flux of the i th spaxel, V_i is the stellar velocity in km s^{-1} and σ_i the velocity dispersion in km s^{-1} . We sum over all spaxels N_{spx} that meet the following quality cut¹¹: signal-to-noise (S/N) $> 3 \text{ \AA}^{-1}$, $\sigma_{\text{obs}} > \text{FWHM}_{\text{instr}}/2 \sim 35 \text{ km s}^{-1}$ where the FWHM is the instrumental spectral full-width at half-maximum, $V_{\text{error}} < 30 \text{ km s}^{-1}$ and $\sigma_{\text{error}} < (\sigma_{\text{obs}} \times 0.1 + 25 \text{ km s}^{-1})$. For galaxies where the largest aperture radius measurement is less than one R_e ($\sim 15\%$ of the total sample), the $(V/\sigma)_e$ measurements are aperture corrected¹⁵⁰ to one R_e .

Stellar populations. Luminosity-weighted stellar population ages are estimated using 11 Lick indices in the SAMI blue spectral range¹². For each aperture spectrum, we first construct an emission-corrected spectrum using a similar approach as the stellar kinematic fits. In series of three pPXF fits, a smoothed noise spectrum is created, which is then used to identify regions of bad pixels or emission lines using the CLEAN keyword in pPXF. These flagged pixels are replaced with corresponding pixels in the best-fitting template spectrum. The emission-corrected observed spectrum is then shifted to a rest-frame wavelength scale based on the measured velocity. Due to the different spectral resolution of each Lick index, we convolve the observed spectrum with a Gaussian, such that the total broadening of the spectrum matches that of the Lick system. In practice, $\sigma_{\text{instrument}}^2 + \sigma_{\text{galaxy}}^2 + \sigma_{\text{applied}}^2 = \sigma_{\text{Lick}}^2$, where $\sigma_{\text{instrument}}$ is the instrumental broadening, σ_{galaxy} is the velocity broadening due to each galaxies intrinsic velocity dispersion, σ_{applied} is the additional broadening applied to each spectrum to match the Lick resolution and σ_{Lick} is the broadening of each index in the Lick system. Uncertainties on all indices are estimated in a similar fashion as the stellar kinematic uncertainties using a 100 simulated spectra using a Monte Carlo procedure.

Lick indices are converted into single stellar population equivalent age using stellar population synthesis models⁵¹ that predict Lick indices as a function of $\log(\text{age})$, metallicity $[Z/H]$ and $[\alpha/\text{Fe}]$. For each aperture spectrum, we use a χ^2 minimization approach to determine the single-burst stellar population (SSP)

that best reproduces the measured Lick indices. In the three-dimensional space of age, $[Z/H]$ and $[\alpha/Fe]$, we adopt the values that result in the minimum χ^2 , and uncertainties on the three SSP parameters are determined from the χ^2 distribution. Typical uncertainties are ± 0.15 in $\log(\text{age})$, ± 0.17 in $[Z/H]$ and ~ 0.14 in $[\alpha/Fe]$.

We caution that our luminosity-weighted SSP-equivalent ages are likely to be biased to young ages (relative to mass-weighted values) for all galaxies that have experienced recent star formation, as we do not account for differing star formation histories, beyond varying $[\alpha/Fe]$. However, the relative differences in SSP-equivalent ages between galaxies are robust and reflect real differences in stellar populations. For early-type galaxies, on average, the SSP-derived ages are lower by 0.2 dex in $\log(\text{age})$ (Gyr) than mass-weighted ages³². However, as the offset between luminosity-weighted and mass-weighted age follows a linear relation with little scatter, this implies that our conclusion will not change if mass-weighted ages are used.

Code availability. The data reduction package used to process the SAMI data is available at <http://ascl.net/1407.006>, and makes use of 2dfdr: <http://www.aao.gov.au/science/software/2dfdr>. To derive the stellar kinematic parameters and the Lick absorption-line strengths, we used the publicly available penalized pixel-fitting (pPXF) code from M. Cappellari: <http://www-astro.physics.ox.ac.uk/~mxc/software/#ppxf>. For the adaptive LOESS smoothing, we use the code from M. Cappellari obtained from <http://www-astro.physics.ox.ac.uk/~mxc/software/#loess>.

Data availability. All reduced data cubes in the GAMA fields used in this paper are available on <http://datacentral.aao.gov.au/asvo/surveys/sami/> as part of the first SAMI Galaxy Survey data release³³. Stellar kinematic and stellar population data products will become available in the second SAMI Galaxy Survey data release. The data that support the plots within this paper and other findings of this study are available from the corresponding author upon reasonable request.

Received: 25 July 2017; Accepted: 1 March 2018;

References

- Tinsley, B. M. Evolution of the stars and gas in galaxies. *Fundam. Cosm. Phys.* **5**, 287–388 (1980).
- Davies, R. L., Efstathiou, G., Fall, S. M., Illingworth, G. & Schechter, P. L. The kinematic properties of faint elliptical galaxies. *Astrophys. J.* **266**, 41–57 (1983).
- Bender, R., Burstein, D. & Faber, S. M. Dynamically hot galaxies. II. Global stellar populations. *Astrophys. J.* **411**, 153–169 (1993).
- Cappellari, M. Structure and kinematics of early-type galaxies from integral field spectroscopy. *Annu. Rev. Astron. Astrophys.* **54**, 597–665 (2016).
- Naab, T. et al. The ATLAS^{3D} project—XXV. Two-dimensional kinematic analysis of simulated galaxies and the cosmological origin of fast and slow rotators. *Mon. Not. R. Astron. Soc.* **444**, 3357–3387 (2014).
- Croom, S. M. et al. The Sydney-AAO Multi-object Integral field spectrograph. *Mon. Not. R. Astron. Soc.* **421**, 872–893 (2012).
- Bundy, K. et al. Overview of the SDSS-IV MaNGA Survey: mapping nearby galaxies at Apache Point Observatory. *Astrophys. J.* **798**, 7 (2015).
- Cappellari, M. et al. The ATLAS^{3D} project—I. A volume-limited sample of 260 nearby early-type galaxies: science goals and selection criteria. *Mon. Not. R. Astron. Soc.* **413**, 813–836 (2011).
- Sánchez, S. F. et al. CALIFA, the Calar Alto Legacy Integral Field Area survey. I. Survey presentation. *Astron. Astrophys.* **538**, A8 (2012).
- Ma, C.-P. et al. The MASSIVE Survey. I. A volume-limited integral-field spectroscopic study of the most massive early-type galaxies within 108 Mpc. *Astrophys. J.* **795**, 158 (2014).
- van de Sande, J. et al. The SAMI Galaxy Survey: revisiting galaxy classification through high-order stellar kinematics. *Astrophys. J.* **835**, 104 (2017).
- Scott, N. et al. The SAMI Galaxy Survey: global stellar populations on the size–mass plane. *Mon. Not. R. Astron. Soc.* **472**, 2833–2855 (2017).
- Binney, J. Rotation and anisotropy of galaxies revisited. *Mon. Not. R. Astron. Soc.* **363**, 937–942 (2005).
- Cappellari, M. et al. The SAURON project—X. The orbital anisotropy of elliptical and lenticular galaxies: revisiting the $(V/\sigma, \epsilon)$ diagram with integral-field stellar kinematics. *Mon. Not. R. Astron. Soc.* **379**, 418–444 (2007).
- Cappellari, M. et al. The ATLAS^{3D} project—XX. Mass-size and mass- σ distributions of early-type galaxies: bulge fraction drives kinematics, mass-to-light ratio, molecular gas fraction and stellar initial mass function. *Mon. Not. R. Astron. Soc.* **432**, 1862–1893 (2013).
- Lange, R. et al. Galaxy And Mass Assembly (GAMA): M_* – R_e relations of $z = 0$ bulges, discs and spheroids. *Mon. Not. R. Astron. Soc.* **462**, 1470–1500 (2016).
- Emsellem, E. et al. The ATLAS^{3D} project—III. A census of the stellar angular momentum within the effective radius of early-type galaxies: unveiling the distribution of fast and slow rotators. *Mon. Not. R. Astron. Soc.* **414**, 888–912 (2011).
- Foster, C. et al. The SAMI Galaxy Survey: the intrinsic shape of kinematically selected galaxies. *Mon. Not. R. Astron. Soc.* **472**, 966–978 (2017).
- Kormendy, J. & Kennicutt, R. C. Jr. Secular evolution and the formation of pseudobulges in disk galaxies. *Annu. Rev. Astron. Astrophys.* **42**, 603–683 (2004).
- Seidel, M. K. et al. The BaLROG project—I. Quantifying the influence of bars on the kinematics of nearby galaxies. *Mon. Not. R. Astron. Soc.* **451**, 936–973 (2015).
- van Dokkum, P. G. et al. Forming compact massive galaxies. *Astrophys. J.* **813**, 23 (2015).
- van der Wel, A. et al. 3D-HST+CANDELS: the evolution of the galaxy size–mass distribution since $z = 3$. *Astrophys. J.* **788**, 28 (2014).
- Newman, A. B., Belli, S. & Ellis, R. S. Discovery of a strongly lensed massive quiescent galaxy at $z = 2.636$: spatially resolved spectroscopy and indications of rotation. *Astrophys. J. Lett.* **813**, L7 (2015).
- Penoyre, Z., Moster, B. P., Sijacki, D. & Genel, S. The origin and evolution of fast and slow rotators in the Illustris simulation. *Mon. Not. R. Astron. Soc.* **468**, 3883–3906 (2017).
- Bland-Hawthorn, J. & Gerhard, O. The galaxy in context: structural, kinematic, and integrated properties. *Annu. Rev. Astron. Astrophys.* **54**, 529–596 (2016).
- Lee, Y. S. et al. Formation and evolution of the disk system of the Milky Way: $[\alpha/Fe]$ ratios and kinematics of the SEGUE G-dwarf sample. *Astrophys. J.* **738**, 187 (2011).
- Sharma, S. et al. Kinematic modeling of the Milky Way using the RAVE and GCS stellar surveys. *Astrophys. J.* **793**, 51 (2014).
- Schönrich, R. & Binney, J. Chemical evolution with radial mixing. *Mon. Not. R. Astron. Soc.* **396**, 203–222 (2009).
- Förster Schreiber, N. M. et al. The SINS Survey: SINFONI integral field spectroscopy of $z \sim 2$ star-forming galaxies. *Astrophys. J.* **706**, 1364–1428 (2009).
- Tacconi, L. J. et al. Phibss: molecular gas content and scaling relations in $z \sim 1$ –3 massive, main-sequence star-forming galaxies. *Astrophys. J.* **768**, 74 (2013).
- Wisnioski, E. et al. The KMOS^{3D} Survey: design, first results, and the evolution of galaxy kinematics from $0.7 < z < 2.7$. *Astrophys. J.* **799**, 209 (2015).
- Bland-Hawthorn, J. et al. Hexabundles: imaging fiber arrays for low-light astronomical applications. *Opt. Express* **19**, 2649 (2011).
- Bryant, J. J., Bland-Hawthorn, J., Fogarty, L. M. R., Lawrence, J. S. & Croom, S. M. Focal ratio degradation in lightly fused hexabundles. *Mon. Not. R. Astron. Soc.* **438**, 869–877 (2014).
- Sharp, R. et al. Performance of AAOmega: the AAT multi-purpose fiber-fed spectrograph. *Proc.* **6269**, 62690G (2006).
- Bryant, J. J. et al. The SAMI Galaxy Survey: instrument specification and target selection. *Mon. Not. R. Astron. Soc.* **447**, 2857–2879 (2015).
- Driver, S. P. et al. Galaxy and Mass Assembly (GAMA): survey diagnostics and core data release. *Mon. Not. R. Astron. Soc.* **413**, 971–995 (2011).
- Owers, M. S. et al. The SAMI Galaxy Survey: the cluster redshift survey, target selection and cluster properties. *Mon. Not. R. Astron. Soc.* **468**, 1824–1849 (2017).
- Sharp, R. et al. The SAMI Galaxy Survey: cubism and covariance, putting round pegs into square holes. *Mon. Not. R. Astron. Soc.* **446**, 1551–1566 (2015).
- Allen, J. T. et al. The SAMI Galaxy Survey: early data release. *Mon. Not. R. Astron. Soc.* **446**, 1567–1583 (2015).
- Emsellem, E., Monnet, G. & Bacon, R. The multi-Gaussian expansion method: a tool for building realistic photometric and kinematical models of stellar systems I. The formalism. *Astron. Astrophys.* **285**, 739–750 (1994).
- Cappellari, M. Efficient multi-Gaussian expansion of galaxies. *Mon. Not. R. Astron. Soc.* **333**, 400–410 (2002).
- Scott, N. et al. The SAURON Project—XIV. No escape from V_{esc} : a global and local parameter in early-type galaxy evolution. *Mon. Not. R. Astron. Soc.* **398**, 1835–1857 (2009).
- York, D. G. et al. The Sloan Digital Sky Survey: technical summary. *Astron. J.* **120**, 1579–1587 (2000).
- Shanks, T. et al. VST ATLAS first science results. *Messenger* **154**, 38–40 (2013).
- Cortese, L. et al. The SAMI Galaxy Survey: the link between angular momentum and optical morphology. *Mon. Not. R. Astron. Soc.* **463**, 170–184 (2016).
- Taylor, E. N. et al. Galaxy And Mass Assembly (GAMA): stellar mass estimates. *Mon. Not. R. Astron. Soc.* **418**, 1587–1620 (2011).
- Chabrier, G. Galactic stellar and substellar initial mass function. *Publ. Astron. Soc. Pac.* **115**, 763–795 (2003).
- Cappellari, M. & Emsellem, E. Parametric recovery of line-of-sight velocity distributions from absorption-line spectra of galaxies via penalized likelihood. *Publ. Astron. Soc. Pac.* **116**, 138–147 (2004).

49. Sánchez-Blázquez, P. et al. Medium-resolution Isaac Newton Telescope library of empirical spectra. *Mon. Not. R. Astron. Soc.* **371**, 703–718 (2006).
50. van de Sande, J. et al. The SAMI Galaxy Survey: revising the fraction of slow rotators in IFS galaxy surveys. *Mon. Not. R. Astron. Soc.* **472**, 1272–1285 (2017).
51. Schiavon, R. P. Population synthesis in the blue. IV. Accurate model predictions for Lick indices and UV colors in single stellar populations. *Astrophys. J. Suppl.* **171**, 146–205 (2007).
52. McDermid, R. M. et al. The ATLAS^{3D} Project—XXX. Star formation histories and stellar population scaling relations of early-type galaxies. *Mon. Not. R. Astron. Soc.* **448**, 3484–3513 (2015).
53. Green, A. W. et al. The SAMI Galaxy Survey: Data Release One with emission-line physics value-added products. *Mon. Not. R. Astron. Soc.* **475**, 716–734 (2018).

Acknowledgements

The SAMI Galaxy Survey is based on observations made at the Anglo-Australian Telescope. The Sydney–Australian Astronomical Observatory Multi-object Integral field spectrograph (SAMI) was developed jointly by the University of Sydney and the Australian Astronomical Observatory. The SAMI input catalogue is based on data taken from the Sloan Digital Sky Survey, the GAMA Survey and the VST ATLAS Survey. The SAMI Galaxy Survey is funded by the Australian Research Council Centre of Excellence for All-sky Astrophysics (CAASTRO), through project number CE110001020, and other participating institutions. The SAMI Galaxy Survey website is <http://sami-survey.org/>. Parts of this research were conducted by the Australian Research Council Centre of Excellence for All-sky Astrophysics in 3 Dimensions (ASTRO 3D), through project number CE170100013. J.v.d.S. is funded under Bland-Hawthorn’s Australian Research Council Laureate Fellowship (FL140100278). N.S. acknowledges support of a University of Sydney Postdoctoral Research Fellowship. S.B. acknowledges the funding support

from the Australian Research Council through a Future Fellowship (FT140101166). M.S.O. acknowledges the funding support from the Australian Research Council through a Future Fellowship (FT140100255). J.v.d.S. and N.S. thank all SAMI team members for valuable discussions. A.M.M. is a Hubble Fellow.

Author contributions

J.v.d.S. and N.S. led the interpretation. J.v.d.S. measured the stellar kinematic parameters from the SAMI Galaxy Survey spectra and wrote the text. N.S. measured the Lick indices from the spectra, and derived the stellar population ages. F.E. measured the structural parameters. All authors contributed to the analysis and interpretation of the data, and contributed to overall team operations, including target catalogue and observing preparation, instrument maintenance, observing at the telescope, writing data reduction and analysis software, managing various pieces of team infrastructure such as the website and data storage systems, and innumerable other tasks critical to the preparation and presentation of a large dataset presented here.

Competing interests

The authors declare no competing interests.

Additional information

Supplementary information is available for this paper at <https://doi.org/10.1038/s41550-018-0436-x>.

Reprints and permissions information is available at www.nature.com/reprints.

Correspondence and requests for materials should be addressed to J.v.

Publisher’s note: Springer Nature remains neutral with regard to jurisdictional claims in published maps and institutional affiliations.